



## Detection of the whole myocardium in 2D-echocardiography for multiple orientations using a geometrically constrained level-set

T. Dietenbeck<sup>a,\*</sup>, M. Alessandrini<sup>b</sup>, D. Barbosa<sup>a,c</sup>, J. D'hooge<sup>c</sup>, D. Friboulet<sup>a</sup>, O. Bernard<sup>a</sup>

<sup>a</sup> Université de Lyon, CREATIS, CNRS UMR5220, INSERM U1044, Université Lyon 1, INSA-LYON, France

<sup>b</sup> ARCES, Università di Bologna, Bologna, Italy

<sup>c</sup> Cardiovascular Imaging and Dynamics, Katholieke Universiteit Leuven, Leuven, Belgium

### ARTICLE INFO

#### Article history:

Received 8 February 2011

Received in revised form 14 October 2011

Accepted 21 October 2011

Available online 31 October 2011

#### Keywords:

Segmentation

Active contour

Hyperquadrics

Echocardiography

### ABSTRACT

The segmentation of the myocardium in echocardiographic images is an important task for the diagnosis of heart disease. This task is difficult due to the inherent problems of echographic images (*i.e.* low contrast, speckle noise, signal dropout, presence of shadows). In this article, we propose a method to segment the whole myocardium (endocardial and epicardial contours) in 2D echographic images. This is achieved using a level-set model constrained by a new shape formulation that allows to model both contours. The novelty of this work also lays in the fact that our framework allows to segment the whole myocardium for the four main views used in clinical routine. The method is validated on a dataset of clinical images and compared with expert segmentation.

© 2011 Elsevier B.V. All rights reserved.

### 1. Introduction

Echocardiography is widely used for the diagnosis of heart disease. This diagnosis is based on a visual inspection of the images by an expert cardiologist and the extraction of quantitative measures (such as the ejection fraction, strain and strain-rate). This latter process involves a manual contouring step, which is time-consuming and prone to errors. Indeed, the low SNR of ultrasound scans is associated to subjective contouring from the experts, which results in significant inter- and intra-observer variability in the delineation of the myocardial borders. In order to avoid this and to speed up the exam analysis workflow, an automatic segmentation procedure is highly desirable.

While great attention has been given to the segmentation of the endocardial wall (Noble and Boukerroui, 2006; Mignotte et al., 2001; Tao and Tagare, 2007; Duan et al., 2009; Carneiro et al., 2010), very limited literature (Dias and Leita, 1996; Chalana et al., 1996) deals with the segmentation of the epicardial wall or the whole myocardium in 2D echocardiography. Let us however note that epicardial segmentation has recently received more attention in 3D echocardiography. In Zhu et al. (2010), such 3D acquisitions allow constraining myocardial segmentation through an incompressibility constraint. A subject-specific dynamical shape prior built from MRI data is introduced in Zhu et al. (2009) in order to segment myocardium from 3D echocardiographic sequences. In Orderud et al.

(2008), coupled segmentation of endo- and epicardial borders is performed by using a Kalman filter-based tracking framework.

The difficulty in segmenting the epicardial border is linked to the fact that the Contrast to Noise Ratio (CNR) between the epicardium and surrounding tissue is lower than the CNR between the endocardium and the blood pool, which usually leads to high heterogeneities in the epicardial contour or missing boundaries. Another difficulty relates to the presence of the papillary muscles on the endocardial borders. Indeed the cardiologists usually do not take these structures into account when delineating the endocardium. Thus, while papillary muscles have similar properties as the myocardium, they typically have to be excluded from the segmentation.

Shape priors have proven to be very efficient in dealing with missing boundaries and papillary muscles (Bosch et al., 2002; Chen et al., 2002; Taron et al., 2004; Paragios et al., 2005; Hamou and El-Sakka, 2010; Alessandrini et al., 2010). As compared to 3D shape constraints (Zhu et al., 2009), let us note that the introduction of shape prior in 2D raises a specific problems, in the sense that the shape of the cardiac structures varies a lot according to the selected echographic acquisition view. As a consequence, segmentation methods using shape prior are generally view dependent: methods based on shape learning imply building a specific training database for each view (Bosch et al., 2002; Chen et al., 2002; Paragios et al., 2005), and methods based on geometric shape constraint are adapted to one specific view (Taron et al., 2004; Hamou and El-Sakka, 2010; Alessandrini et al., 2010). One of the main interests of our approach is to provide a framework that can be used for any of the usual 2D echographic views (*i.e.* parasternal short-axis, parasternal long-axis, apical 4-chamber, and apical 2-chamber).

\* Corresponding author.

E-mail address: [thomas.dietenbeck@creatis.insa-lyon.fr](mailto:thomas.dietenbeck@creatis.insa-lyon.fr) (T. Dietenbeck).

(Bosch et al., 2002) used an adaptation of the active appearance model (AAM) approach that they called the active appearance motion model (AAMM) to represent the shape and appearance of the endocardium, as well as its motion, but their method was only tested on apical 4-chamber views.

(Paragios et al., 2005) proposed a parametric curve model dedicated to the extraction of the endocardium for each frame of a cine-loop cardiac cycle. First a training step was performed where the shape model was built from a linear combination of a diastolic and a systolic model obtained from a Principal Components Analysis (PCA) applied to registered curves. Then the segmentation step consisted of two main steps. First an approximate segmentation of the left ventricle for each image in the sequence was performed. This allowed registering the shape model in each frame by recovering the parameters of a similarity transformation. The segmentation was subsequently refined using the approximate segmentation as an initial solution. The ability of the method for the segmentation and tracking of the endocardium was tested on apical 4-chamber views.

Based on their previous work (Chen et al., 2002, 2007) were able to segment either the endocardium or the epicardium in apical 4-chamber views (A4C). They used the intensity gradient of the *B*-mode images and a distance measure between the evolving contour and a learned shape to drive the level-set function towards the object boundaries. The shape prior was obtained by averaging aligned contours drawn by an expert. Multiple segmentations of the same images were performed, where the weighting parameter between those two terms was changed. Finally, the intensity profile along the segmentation result was compared to a learned intensity profile in order to choose the best weighting parameter and thus the best contour.

The main drawback of these techniques is that the shape knowledge is often learned via an interactive training process. Though this training process can take place off-line, this involves considerable effort and expertise. More importantly, a learned shape template can only be used to segment a specific class of images with similar boundary shape and will therefore be highly dependent on the probe orientation.

In order to avoid shape learning, (Taron et al., 2004) proposed a method for the recovery of the endocardium in parasternal short-axis view using a geometric model. This approach relies on the assumption that the endocardial contour in a parasternal short-axis view can be reliably modelled as an ellipse. The contour evolution then corresponds to deforming an ellipse according to its parameters, so it is attracted to the desired image features. Though this method does not require any learning step, the shape prior used might be too strong and cannot be applied to other views where the myocardial border does not correspond to an ellipse.

(Lin et al., 2003) used a multiscale framework, where the result at a coarse level was used as an initialisation and shape prior at a finer level. The algorithm was then used to segment the endocardium in apical 4-chamber images. More recently, (Hamou and El-Sakka, 2010) used a geometrical model based on third-order hyperbolas to constraint the shape of the evolving contour and improve the segmentation of the endocardium in apical 4-chamber images. (Alessandrini et al., 2010) improved the level-set method of Alessandrini et al. (2009) by incorporating an annular shape prior into the energy minimization in order to segment the whole myocardium in parasternal short-axis views.

The novelties introduced in this paper are the following.<sup>1</sup> We propose to segment the whole myocardium (endocardium and epi-

cardium) for all the four main clinical orientations of acquisition (i.e. Parasternal short and long axis and Apical two and four chamber views) using one single level-set. First, the level-set is constrained through a shape prior based on the combination of two hyperquadrics. We indeed show from real data that this hyperquadrics prior is general enough to efficiently approximate the shape of the myocardium in each clinical orientation, due to its ability to handle asymmetries. This constraint is formalized in a variational framework using the geodesic formulation initially described by Caselles et al. (1997) for data attachment terms. The interest of such formulation stems from the fact that the associated minimization can be shown to correspond to a simple least-square problem with respect to the parameters defining the prior. We then show that the problem of performing the least-square fitting of a pair of hyperquadrics is formally equivalent to solve two separate simple fitting problems. An additional benefit of this approach is that it does not involve any learning procedure, since the prior is purely geometric. Secondly, the formulation of the whole myocardium segmentation using one single level-set also allows introducing of a new thickness energy term in a variational framework. The proposed formulation ensures that both contours of our single level-set function will not merge while still allowing the myocardium thickness to vary.

The paper is organized as follows. In Section 2, we recall the general level-set framework and describe the energy functional that will be minimized. In Section 3, we detail the method to fit the shape prior on the evolving contour. Implementation issues are discussed in Section 4. Section 5 is devoted to the results obtained from echocardiographic clinical images and a comparison with Hamou's method (Hamou and El-Sakka, 2010). We give the main conclusions and perspectives in Section 6.

## 2. Proposed method

We now describe the framework used to segment the whole myocardium in 2D echocardiography. Though many segmentation techniques exist, we choose to focus on level-set *s*, which are now a well-established and popular tool in the field of image processing. Level-sets correspond to a class of deformable models where the shape to be recovered is captured by propagating an interface represented by the zero level-set of a smooth function which is usually called the level-set function. The evolution of the interface is generally derived through a variational formulation: the segmentation problem is expressed as the minimization of an energy functional that reflects the properties of the objects to be recovered (Osher and Sethian, 1988). Moreover the segmentation process is expressed in an Eulerian framework. This removes the problem of contour self-intersections and the need for control point regriding mechanisms.

### 2.1. Level-set framework

Let  $\Omega \in \mathbb{R}^2$  denotes the image space. In the level-set formalism, the evolving interface  $\Gamma \in \mathbb{R}^2$  is represented as the zero level-set of a Lipschitz-continuous function  $\phi : \Omega \rightarrow \mathbb{R}$ . The problem of segmenting one object from the background is then handled by the evolution of one level-set driven by the minimization of a specific energy criterion; its steady state partitions the image into two regions that delimit the boundaries of the object to be segmented.

Since we are addressing the segmentation of the whole myocardium, which is bounded by two unconnected contours, we describe in the sequel an approach which will yield one level-set having two contours as shown in Fig. 1.

<sup>1</sup> A preliminary version of this work appeared in Dietenbeck et al. (2011). The present paper describes in detail the formal aspects and the behavior of the proposed method, evaluates the performances from a data set including 80 medical images and compares it to the shape prior-based algorithm of Hamou and El-Sakka (2010).

## 2.2. Energy formulation

As mentioned in the introduction, many energy functionals have been proposed in literature to incorporate shape priors into the level-set formulation. Usually, the authors sum two energy terms: a data attachment term and the shape prior one (Leventon et al., 2000; Chen et al., 2002; Alessandrini et al., 2010). Here, since we consider the simultaneous segmentation of two unconnected contours, we also include an anti-collision term. We thus adopt the following general expression for the energy functional:

$$E = E_{data} + E_{thickness} + E_{shape}, \quad (1)$$

where  $E_{data}$  represents the chosen data attachment term,  $E_{thickness}$  is a term that prevents the contours from merging by imposing a minimum thickness and  $E_{shape}$  embeds the shape prior.

## 2.3. Data attachment term

Intensity inhomogeneities often appear along the myocardial boundaries as shown in Fig. 2. In Fig. 2a, due to a loss of contrast, intensity inhomogeneity appears between the lateral wall (area 1) and the anterior wall (area 2). In Fig. 2b, the apex (area 1) is blurred and less contrasted than the septum wall (area 2) because it is located in the near field of the probe.

In order to cope with these intensity inhomogeneities, (Lankton and Tannenbaum, 2008) recently proposed a general framework to localize the data attachment term. Though more sophisticated attachment terms could be used, we adopt the localized version of the Chan–Vese model (Chan and Vese, 2001), as data attachment term  $E_{data}$  and computed directly from the B-mode scan. This formulation handles local statistics and is therefore well suited for segmenting objects whose boundaries are discontinuous or heterogeneous, where standard region based methods that use global statistics fail.

Using the general framework described in Lankton and Tannenbaum (2008), the data attachment term  $E_{data}$  can be written as

$$E_{data}(\phi) = \int_{\Omega} \delta(\phi(\mathbf{x})) \int_{\Omega} B(\mathbf{x}, \mathbf{y}) F(I, \phi, \mathbf{y}) d\mathbf{y} d\mathbf{x}, \quad (2)$$

where  $F(I, \phi, \mathbf{y}) = H(\phi(\mathbf{y})) \cdot (I(\mathbf{y}) - u_x)^2 + (1 - H(\phi(\mathbf{y}))) \cdot (I(\mathbf{y}) - v_x)^2$  and  $\delta(\cdot)$  is the Dirac function. The function  $B(\cdot)$  is a binary mask defined as

$$B(\mathbf{x}, \mathbf{y}) = \begin{cases} 1, & \text{if } \mathbf{y} \in N(\mathbf{x}) \\ 0, & \text{otherwise} \end{cases} \quad (3)$$

where  $\mathbf{y}$  is a spatial variable that represents a single point in  $\Omega$  and  $N(\mathbf{x})$  corresponds to a user-defined neighborhood of point  $\mathbf{x}$ . The quantities  $u_x$  and  $v_x$  correspond to the localized version of the inside and outside average intensity values measured in the window  $N(\mathbf{x})$ .

Minimizing  $E_{data}$  (2) with respect to  $\phi$  leads to the following level-set equation:

$$\frac{\partial \phi}{\partial t}(\mathbf{x}) = -\delta(\phi(\mathbf{x})) \cdot \int_{\Omega} B(\mathbf{x}, \mathbf{y}) \nabla_{\phi} F(I, \phi, \mathbf{y}) d\mathbf{y}. \quad (4)$$

From Eq. (4), it is apparent that,  $N(\mathbf{x})$  defines to which extent the algorithm is localized: at each point  $\mathbf{x}$  of the interface, the term driving the evolution is computed only in the neighbourhood  $N(\mathbf{x})$  surrounding  $\mathbf{x}$  (instead of being computed from the whole image, as in the usual level set formulation).

As indicated in Lankton and Tannenbaum (2008) the size of  $N(\mathbf{x})$  is mainly linked to the size of the object to recover: it should be small enough so that the interface is not attracted by nearby structures that are not to be detected (in the limit, if  $N(\mathbf{x})$  is very large, the algorithm is then equivalent to the usual Chan–Vese algorithm and will perform a global segmentation). Conversely if  $N(\mathbf{x})$  is too small, there is a risk that the interface will not move since it is too far from the object borders.

## 2.4. Thickness term

Since we are dealing with the evolution of a shape bounded by two contours, it might happen that they are both attracted by the same image feature, leading to the merging of both contours. In our experiments, we observed that this happened in about 15% of the segmentations. It is thus important to prevent both contours from merging since this leads to results that are not meaningful. How-

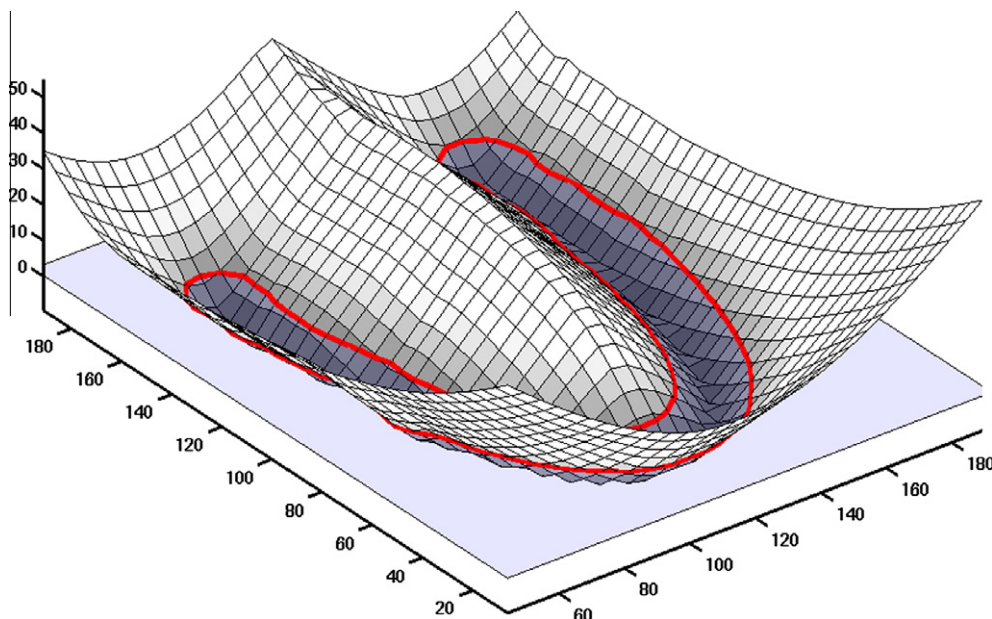
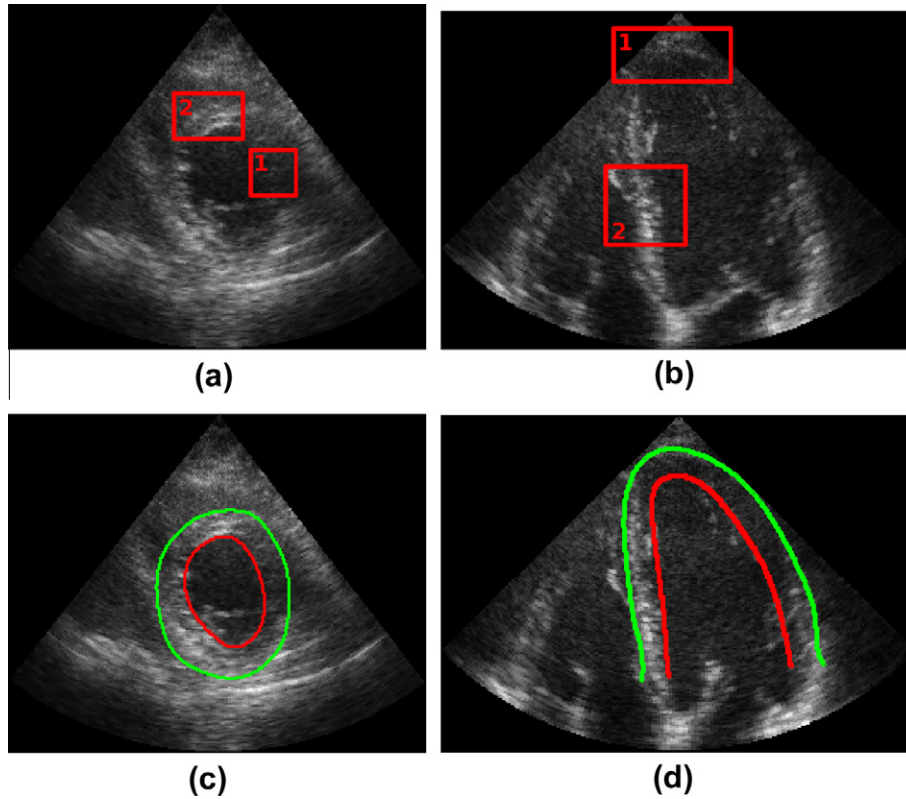


Fig. 1. Example of the level-set function used in this work. The zero level is represented as a red bold line and provides the contour corresponding to the boundary of the myocardium. (For interpretation of the references to colour in this figure legend, the reader is referred to the web version of this article.)



**Fig. 2.** Examples of the intensity inhomogeneities occurring along the myocardium borders. Top row: short-axis view (left) and apical 4-chamber view (right). Bottom row: same images with the cardiologist's reference epicardial (green) and endocardial contours (red). (For interpretation of the references to colour in this figure legend, the reader is referred to the web version of this article.)

ever it is also important to ensure that this will not modify the behavior of the algorithm when there is no merging problem. This is done in our approach by locally constraining the level-set to have a minimum thickness.

The idea of using such a local thickness term to constrain level-set segmentation has been initially proposed by Zeng et al. (1998) for cortex segmentation in MR. This initial approach has then been used for 2D cardiac images in US by Paragios (2002), in MR by Lynch et al. (2006) and tested against incompressibility constraint for 3D cardiac US data in Zhu et al. (2010). In these works, the object to be segmented is modelled as two distinct level-sets and the constraint is directly introduced in the evolution equation as a term coupling the two level-sets. Our approach is different due to the fact that the two contours are represented as a single implicit function. This allows expressing the constraint as an energy to be minimized and thus deriving the corresponding evolution in a variational framework, which depends only on the level-set  $\phi$ . Let us note that (Chen et al., 2008) also recently described a thickness constraint as an energy to be minimized. However, in this formulation the object is modelled as two distinct level-sets and the constraint essentially acts as a global term minimizing the overall deviation from the average thickness of the myocardium. In our formulation the constraint is applied locally, stopping the evolution in the region of the interfaces where the minimum thickness is not met.

Formally, we define the energy term such that it will allow the level-set to evolve only if the distance between the inner and outer contour is lower than a predefined thickness  $R_T$

$$E_{\text{thickness}}(\phi) = \int_{\Omega} \phi(\mathbf{x} + R_T \mathbf{N}) \cdot H(\phi(\mathbf{x} + R_T \mathbf{N})) \cdot \delta(\phi(\mathbf{x})) \, d\mathbf{x}, \quad (5)$$

where  $\mathbf{N}$  corresponds to the inward normal of a point  $\mathbf{x} \in \Gamma$ . From (5), it is clear that this energy is null when all the point at a distance  $R_T$  along the inward normal of the contours are inside points. Minimizing this energy thus guarantees that the thickness of the contour will be at least  $R_T$  but do not put any constraint on the maximal thickness between the two contours.

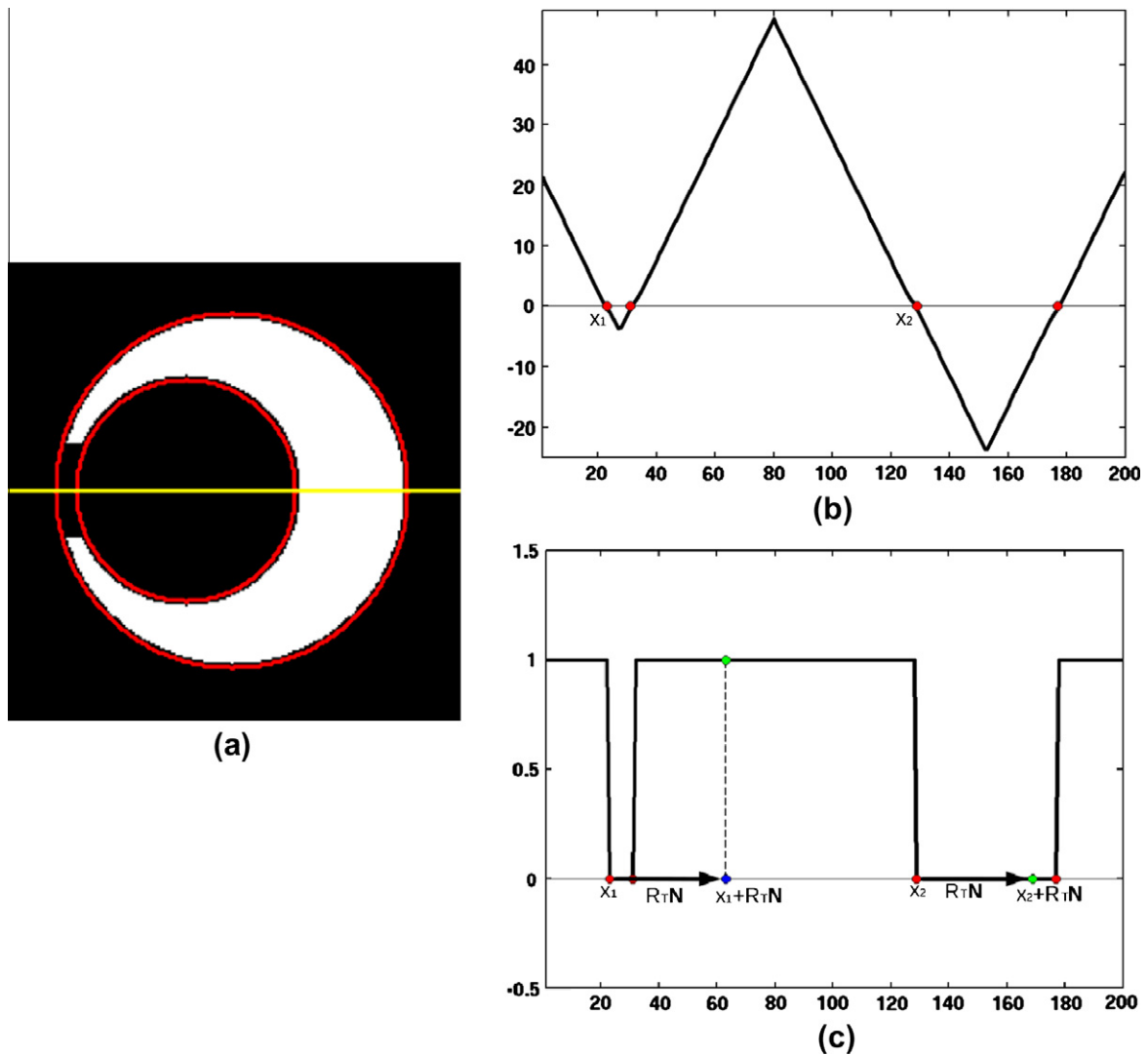
The evolution term is obtained by deriving the Eq. (5) with respect to  $\phi$  and writes as:

$$\frac{\partial \phi}{\partial t}(\mathbf{x}) = -H(\phi(\mathbf{x} + R_T \mathbf{N})) \cdot \delta(\phi(\mathbf{x})). \quad (6)$$

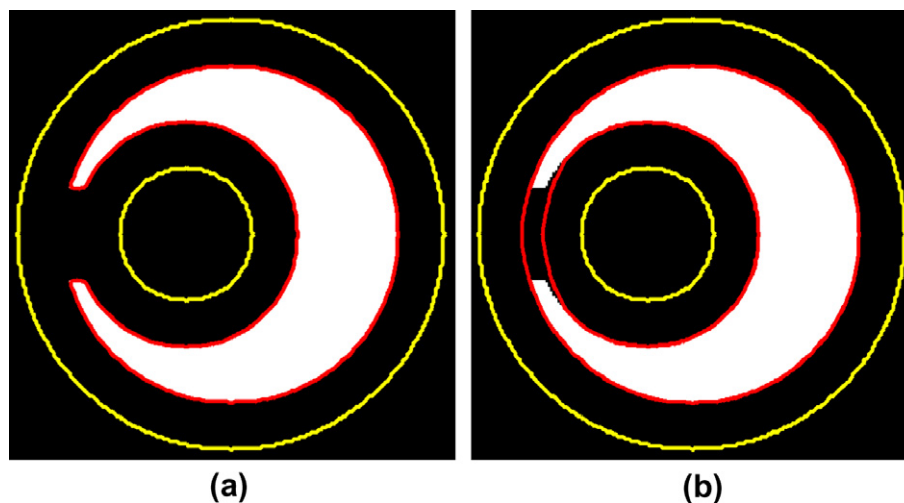
The complete derivation of this term is given in Appendix A.

Fig. 3 illustrates the principle of this term. In Fig. 3a, we show a simulated image composed of two disks, one inside the other. The centers of the disks are not the same and thus the thickness of the object is not homogeneous. The left part of the object has been occluded in order to mimic a loss of contrast that may occur in echocardiographic scans. We also show the zero-level of  $\phi$  at a point in the evolution process where the inner and outer contour are about to merge. Fig. 3b shows a 1D profile of  $\phi$  along the yellow line seen in Fig. 3a while Fig. 3c shows the corresponding Heaviside function  $H(\phi)$ . In Fig. 3c, at point  $\mathbf{x}_2$ , the distance between the two contours (red points) is higher than  $R_T$ . Thus  $\mathbf{x}_2 + R_T \mathbf{N}$  is an inside point,  $H(\phi(\mathbf{x}_2 + R_T \mathbf{N}))$  is equal to 0 and so is the thickness evolution term (6). On the opposite for the point  $\mathbf{x}_1$ , the two contours are too close, the value of  $H(\phi(\mathbf{x}_2 + R_T \mathbf{N}))$  is equal to 1, and the level-set will thus evolve according to (6). It is therefore apparent that the energy (5), will be minimized (and equal to 0) when the distance between the contours is at least  $R_T$ .

Fig. 4 shows the final segmentation of the image shown in Fig. 3a. In this illustrative binary image example, we use the clas-



**Fig. 3.** Principle of the thickness term: (a) simulated image with the zero-level of an evolving level-set  $\phi$  shown in red; (b) 1D-profile of  $\phi$  along the yellow line of (a); (c)  $H(\phi)$ . In (b) and (c) the red dots corresponds to the zero-level of  $\phi$ . The blue points in (c) correspond to points at a distance  $R$  from  $x_1$  and  $x_2$  with their respective value of  $H(\phi)$  shown as the green dots. (For interpretation of the references to colour in this figure legend, the reader is referred to the web version of this article.)



**Fig. 4.** Segmentation results on the same image as Fig. 3a, (a) without the thickness term and (b) with the thickness term. The initialisation is shown in yellow and the segmentation result in red. (For interpretation of the references to colour in this figure legend, the reader is referred to the web version of this article.)

sical Chan–Vese data attachment term (Chan and Vese, 2001) and no shape prior. Fig. 4a gives the result obtained without the thickness term. In that case, since the left part of the image is occluded, the two evolving contours merge, leading to an unsatisfactory segmentation result. On the contrary, by including the thickness term in the evolution equation, the merging of the two contours does not occur yielding the desired segmentation (Fig. 4b).

### 3. Shape prior term

Many shape prior energies have been proposed in the literature to constrain the level-set function to remain close to a desired shape. As mentioned in Section 1, the main drawback of most of these techniques is that a training process is required in order to obtain the shape prior. Moreover a learned shape can only be used on a specific orientation, making the algorithm view dependent.

We are thus interested in finding a simple model that could be applied to any view while reliably approximating the heart boundaries. In this context, (Hamou and El-Sakka, 2010) proposed a simple parametric representation to model the endocardium in apical 4-chamber views. The evolving contour is divided into an upper region and a lower region, which are then approximated by two separate third-order hyperbolas to build the shape prior. As will be shown in Section 5, this model can only be applied reliably to apical views and has difficulties to approximate contours drawn by experts in the other orientations.

We thus propose to use a new shape model that can faithfully approximate the myocardial shape whatever the view. This is achieved by modelling each of the two contours by hyperquadrics. Since the seminal work of Hanson (1988), hyperquadrics have been often used in pattern recognition (Kumar et al., 1995; Cohen and Cohen, 1996). In the particular field of biomedical image analysis they have been used for segmentation of cell nuclei (Cong and Parvin, 2000), human thorax (Lelieveldt et al., 1999) and the modelling of the left ventricular shape (Robert, 1995; Cohen and Cohen, 1996; Abdallah et al., 2010). In these works hyperquadrics are used to perform a shape fit on a fixed set of points or features that have already been extracted. Moreover, these approaches do not address the case of an object bounded by two hyperquadrics. In this context, the contributions of our approach are the following:

1. We express the shape constraint through a variational energy term, and we show that the minimization of this term formally corresponds to a shape fitting problem. In contrast with the above mentioned works this approach allows directly embedding the hyperquadrics shape constraint in the level-set evolution process.
2. We then derive a solution to the problem simultaneously fitting two hyperquadrics to a set of points. Based on the formulation from (Berg, 1998), we express the two hyperquadrics as a single implicit function and show that the fitting is formally equivalent to solve two separate fitting problems.

#### 3.1. Shape modelling using hyperquadrics

Hyperquadrics were first proposed for computer graphics applications by (Hanson, 1988). They are obtained by considering a sum of an arbitrary number of linear terms raised to powers and generate convex shapes bounded by a polygon. While even a small number of terms allows to represent a large variety of shapes, increasing this number allows to better approximate complex shapes, making the model very flexible. Moreover hyperquadrics can model shapes that are not necessarily symmetric. This property is interesting in our application since the shape of the endocardium or the epicardium may involve asymmetries (this is illustrated in the results shown in Fig. 9).

In the case of a 2D shape, a hyperquadric implicit function is given by

$$\varphi(x, y) = \sum_{i=1}^{N_h} |A_i x + B_i y + C_i|^{2i}, \quad (7)$$

where  $\lambda = \{A_i, B_i, C_i, \gamma_i, \forall i = 1, \dots, N_h\}$  is the set of parameters to be fitted and  $N_h$  is the number of hyperquadrics terms. The modelled shape corresponds to the set of points  $(x, y)$  that satisfies  $\varphi(x, y) = 1$  and can be represented as the zero level of the implicit function

$$\Psi(\mathbf{x}, \lambda) = \varphi(\mathbf{x}) - 1, \quad (8)$$

where  $\Psi$  is the distance from a point to the hyperquadric.

To fit a hyperquadric to range data, we first define an error-of-fit (EoF) function to measure the difference between a modelled shape and the given data set. Though the distance defined in (8) could be used, the minimization of this EoF function often leads to incorrect results as the EoF function presents multiple global or local minima. Thus, following the work of (Kumar et al., 1995), the hyperquadrics' parameters are fitted by minimizing the following EoF function

$$EoF = \sum_{i=1}^{N_{data}} \frac{1}{\|\nabla F_{io}(x_i, y_i)\|^2} (1 - F_{io}(x_i, y_i))^2 + \nu \sum_{i=1}^N P_i, \quad (9)$$

where  $F_{io}(x, y) = (\varphi(x, y))^p$ ,  $P_i$  is a penalty allowing to avoid degenerate solutions. Eq. (9) thus corresponds to a constrained minimization problem including a data attachment term and a penalization term weighted by  $\nu$ .

As shown in Kumar et al. (1995),  $P_i$  is directly related to the minimum and maximum dimension of the object considered for the fitting (the derivation of  $P_i$  is too long to be detailed here and we refer the reader to (Kumar et al., 1995) for brevity sake). In our application these dimensions have been chosen as the minimum and maximum extent of the myocardium in the echographic images.

Regarding the weighting term  $\nu$ , it can be shown that the solution to the constrained problem (9) coincides with the least square problem when  $\nu$  tends to infinity. In practice, a correct result is obtained for a sufficiently large value of  $\nu$ . In all our experiments,  $\nu$  is set to  $10^8$  so that the penalization term is on the same order than the data attachment term.

The minimization of (9) is accomplished by the Levenberg–Marquardt non-linear optimization method (Press et al., 1992).

#### 3.2. Shape modelling of the myocardium

As will be shown in Section 5.3, each of the myocardial boundaries (*i.e.* the endocardium and the epicardium) can be modelled by a single hyperquadric. We are thus searching for a shape representation that allows: (1) to model these two contours through a single implicit representation, (2) to solve efficiently the fitting problem to update the shape parameters. Let us call  $\psi$  this representation. A trivial choice for  $\psi$  could consist in the pointwise product between two distance functions. However, the resulting representation would no longer be a distance function (Berg, 1998) and, further, it would not allow an optimized solution to the fitting problem, as the one we are presenting in the sequel. Following the work presented in Berg (1998), the shape prior is thus defined as:

$$\psi(\mathbf{x}, \lambda) = \max(\Psi(\mathbf{x}, \lambda_{out}), -\Psi(\mathbf{x}, \lambda_{in})), \quad (10)$$

where  $\lambda = [\lambda_{in}, \lambda_{out}]$  and  $\lambda_{in}$  and  $\lambda_{out}$  represent the parameters of the inner and outer shapes. The function  $\Psi(\cdot)$  corresponds to the distance from a point  $\mathbf{x} = (x, y)$  to a hyperquadric (Eq. (8)). Fig. 5 gives

an illustration of the parametric implicit function  $\psi$  adopted in the proposed framework.

### 3.3. Shape prior energy

Inspired by the framework proposed in Caselles et al. (1997) and Chen et al. (2002), we define a new shape constraint into our level-set framework by minimizing the following shape prior energy:

$$E_{\text{shape}}(\phi, \lambda) = \int_{\Omega} \psi^2(\mathbf{x}, \lambda) \cdot \|\nabla \phi(\mathbf{x})\| \cdot \delta(\phi(\mathbf{x})) d\mathbf{x}, \quad (11)$$

where  $\psi(\mathbf{x}, \lambda)$  is the implicit function representing the distance of a point  $\mathbf{x}$  to the myocardial shape defined by the parameters  $\lambda$ . Clearly (11) reads as a measure of the distance between the active contour and the shape prior, and therefore imposes a similarity between the segmentation result and the prior itself.

The minimization of energy (11) may be interpreted as finding a geodesic zero level-set in a Riemannian space derived from the shape prior content. As compared to the initial work of (Caselles et al., 1997) and derived approaches (Chen et al., 2002), the arc length function of (11) is no longer weighted by an image based information but by our shape prior term. From the observation that the minimum of this expression is reached when the zero level of  $\phi$  perfectly fits the zero level of the parametric implicit function  $\psi$ , one can anticipate that the minimization of this energy criterion will drive the level-set toward a shape composed of two hyperquadrics.

The minimization of (11) is addressed in a two phase scheme. Specifically, keeping  $\lambda$  fixed,  $\phi$  is evolved according to the level-set equation:

$$\frac{\partial \phi}{\partial t}(\mathbf{x}) = \delta(\phi(\mathbf{x})) \cdot \left( \frac{\langle \nabla \psi(\mathbf{x}, \lambda), \nabla \phi(\mathbf{x}) \rangle}{\|\nabla \phi(\mathbf{x})\|} + \psi^2(\mathbf{x}, \lambda) \cdot \kappa \right), \quad (12)$$

where  $\kappa$  is the curvature of the evolving interface and  $\langle \cdot, \cdot \rangle$  denotes the scalar product. Then, keeping  $\phi$  fixed,  $\lambda$  is updated according to the following fitting problem:

$$\lambda = \arg \min_{\lambda'} \int_{\Gamma} \psi^2(\mathbf{x}, \lambda') d\mathbf{x}. \quad (13)$$

As detailed in the sequel, we impose  $\phi$  to be a signed distance map (Osher and Fedkiw, 2002). Thus  $\|\nabla \phi\| = 1$  and (13) corresponds to the exact minimization of (11) w.r.t.  $\lambda$ . In the next section, we propose a fast solution to the fitting problem in (13), which can be employed for implementing efficiently the parameters update step.

Note that, as the image space is in practice discrete, Eq. (13) can be rewritten as:

$$\lambda = \arg \min_{\lambda'} \sum_{\mathbf{x} \in \Gamma} \psi^2(\mathbf{x}, \lambda'). \quad (14)$$

### 3.4. Fast solution to the fitting problem

Considering (10), we can rewrite the sum in (14) as:

$$J(\mathbf{x}, \lambda) = \sum_{\mathbf{x} \in \Gamma_{\text{in}}} \Psi^2(\mathbf{x}, \lambda_{\text{in}}) + \sum_{\mathbf{x} \in \Gamma_{\text{out}}} \Psi^2(\mathbf{x}, \lambda_{\text{out}}), \quad (15)$$

where the partition  $\Gamma = \{\Gamma_{\text{in}}, \Gamma_{\text{out}}\}$  has been introduced

$$\Gamma_{\text{in}}(\lambda_{\text{in}}, \lambda_{\text{out}}) = \{\mathbf{x} \in \Gamma \mid \Psi(\mathbf{x}, \lambda_{\text{out}}) < -\Psi(\mathbf{x}, \lambda_{\text{in}})\}, \quad (16)$$

$$\Gamma_{\text{out}}(\lambda_{\text{in}}, \lambda_{\text{out}}) = \{\mathbf{x} \in \Gamma \mid \Psi(\mathbf{x}, \lambda_{\text{out}}) \geq -\Psi(\mathbf{x}, \lambda_{\text{in}})\}. \quad (17)$$

From this formulation, we observe that (15) can be minimized by fitting two separate hyperquadrics on  $\Gamma_{\text{in}}$  and  $\Gamma_{\text{out}}$ , for which fast direct solvers exist (Eq. (9)). Consequently we propose to minimize  $J$  by alternatively fitting the two hyperquadrics and updating  $\Gamma_{\text{in}}$  and  $\Gamma_{\text{out}}$  according to (16) and (17). The resulting algorithm is summarized in Algorithm 1. By doing so, the energy  $J$  is ensured to decrease at each step. In Algorithm 1 we call fitHQ the function performing the hyperquadric fitting as described in (Kumar et al., 1995).

#### Algorithm 1. Hyperquadric fitting algorithm

---

##### Input data

$$\hat{\lambda}^{(0)\text{in}}, \hat{\lambda}^{(0)\text{out}}, \text{tol} = 0.01, k = 1$$

##### Initialization

$$J^{(0)} = J(\hat{\lambda}^{(0)\text{in}}, \hat{\lambda}^{(0)\text{out}})$$

$$\Gamma^{(0)\text{in}} = \Gamma_{\text{in}}(\hat{\lambda}^{(0)\text{in}}, \hat{\lambda}^{(0)\text{out}}), \quad \Gamma^{(0)\text{out}} = \Gamma_{\text{out}}(\hat{\lambda}^{(0)\text{in}}, \hat{\lambda}^{(0)\text{out}}),$$

##### while $\epsilon > \text{tol}$ do

$$\hat{\lambda}^{(k)\text{in}} = \text{fitHQ}(\Gamma^{(k-1)\text{in}}), \quad \hat{\lambda}^{(k)\text{out}} = \text{fitHQ}(\Gamma^{(k-1)\text{out}}),$$

$$\Gamma^{(k)\text{in}} = \Gamma_{\text{in}}(\hat{\lambda}^{(k)\text{in}}, \hat{\lambda}^{(k)\text{out}}), \quad \Gamma^{(k)\text{out}} = \Gamma_{\text{out}}(\hat{\lambda}^{(k)\text{in}}, \hat{\lambda}^{(k)\text{out}}),$$

$$J^{(k)} = J(\hat{\lambda}^{(k)\text{in}}, \hat{\lambda}^{(k)\text{out}})$$

$$\epsilon = \|J^{(k)} - J^{(k-1)}\| / \|J^{(k-1)}\|, \quad k = k + 1$$

##### end while

---

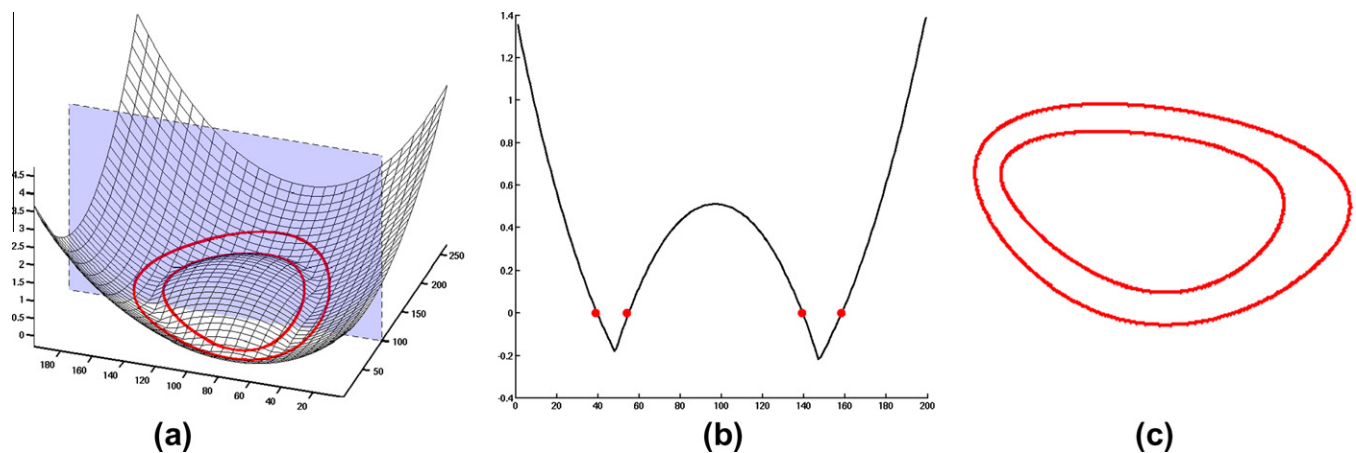


**Fig. 5.** Illustration of the parametric implicit function  $\psi$ . The zero level is represented in red. (a) 3-D representation. (b) Visualization of a 2-D profile corresponding to the color plane given in (a). (c) Visualization of the zero-level of  $\psi$ . (For interpretation of the references to colour in this figure legend, the reader is referred to the web version of this article.)

We remark that, within the segmentation flow, Algorithm 1 is used to fit the points on the evolving contour. In this case, at every time step, the adopted initialisation consists in the two hyperquadrics obtained from fitting the active contour at the previous time step. Since in this interval the displacement of the active contour is expected to be small, such initialisation allows often the convergence to be reached in one single iteration.

In Fig. 6, we show an example of evolution of a level-set using two evolution terms: a data attachment term and the one proposed in (12). Since the image to be segmented is a binary mask with a small gaussian noise, there is no need for a sophisticated data attachment term and we thus use the classical Chan and Vese term (Chan and Vese, 2001). The image contains an object whose boundaries correspond to two hyperquadrics. Though three parts of the object were occluded, we can see that the evolving contour is able to recover the whole object by filling the missing boundaries.

## 4. Implementation issues

### 4.1. Level-set evolution

We implemented our level-set evolution equation using standard finite difference scheme (Osher and Fedkiw, 2002), where the implicit function is represented by a signed distance function  $\phi$ . In order to improve efficiency, we only compute values of  $\phi$  in a narrow band around the zero level-set.

Consequently, we re-initialize  $\phi$  every iteration using a fast marching scheme (Sussman et al., 1998). In order to perform segmentation with a shape prior, the level-set evolves according to the following equation:

$$\frac{\partial \phi}{\partial t} = f(\mathbf{x}) + g(\mathbf{x}) + h(\mathbf{x}), \quad (18)$$

where  $f(\cdot)$  is the data attachment term given in Eq. (4),  $g(\cdot)$  is the thickness term given in Eq. (6) and  $h(\cdot)$  is the shape prior term given in Eq. (12).

As in Lankton and Tannenbaum (2008) the neighbourhood  $N(\mathbf{x})$  defining the localization of the algorithm is chosen in our case as a circular neighbourhood, with radius  $R_N$  (i.e. we assume isotropic

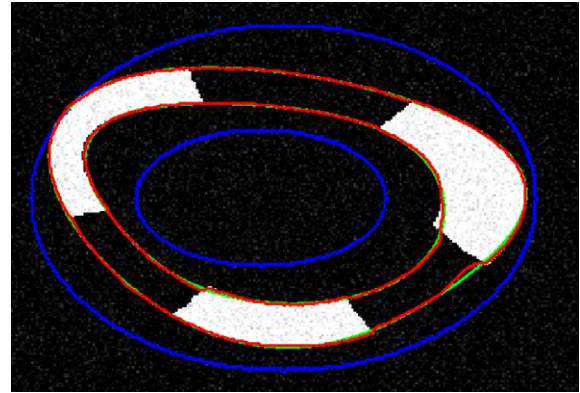


Fig. 6. Illustration of the evolution of a level-set when minimizing the proposed shape prior energy and the classical Chan and Vese data attachment term (Chan and Vese, 2001). In blue, the initial contour; in red, the final contour; in green, the shape prior. (For interpretation of the references to colour in this figure legend, the reader is referred to the web version of this article.)

image properties). Given that we use a close initialisation (i.e. assumed to be on the order of  $R_N$  pixels apart from the desired border),  $R_N$  was thus chosen as the average thickness of the myocardium, i.e. 15 pixels in our case. In the same way, the value of  $R_T$  in the thickness term (5) was chosen to be set to 15 pixels.

### 4.2. Choice of the number of hyperquadrics terms $N_h$

The number of hyperquadrics term  $N_h$  in Eq. (7) is linked to the complexity of the shape that we want to represent. (Kumar et al., 1995) also showed that, in order to have asymmetrical shapes,  $N_h$  has to be greater than 2. We choose to set  $N_h = 4$  since, as we will show in Section 5.3, this allows to model the myocardial border with a good accuracy.

### 4.3. Image subdivision and ROI definition

In parasternal long-axis or apical images, the endocardium or epicardium are not closed contours and are only defined on the left

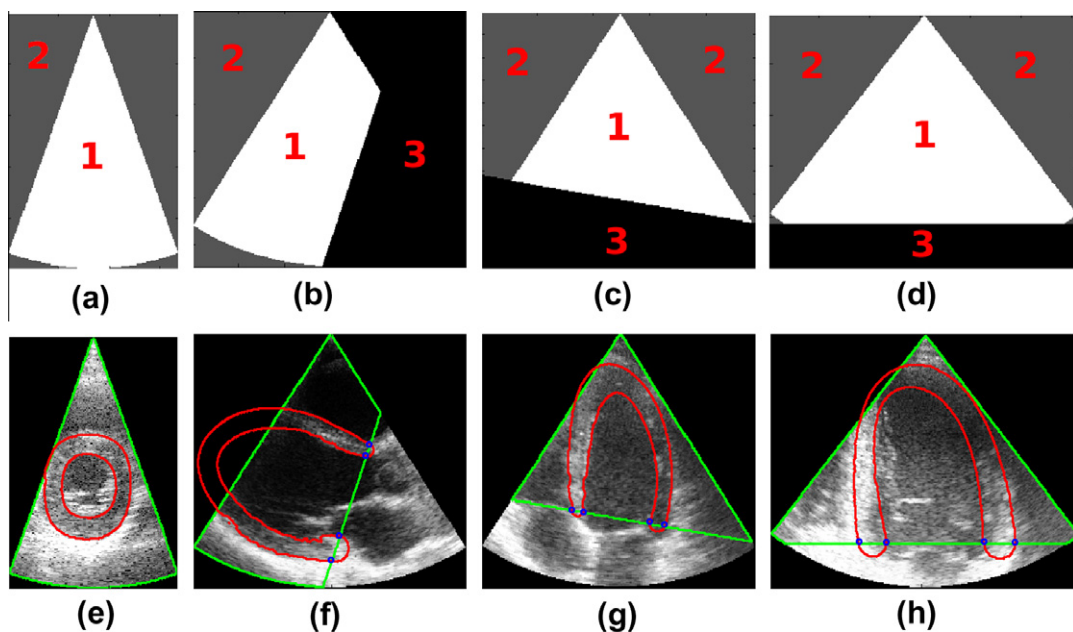
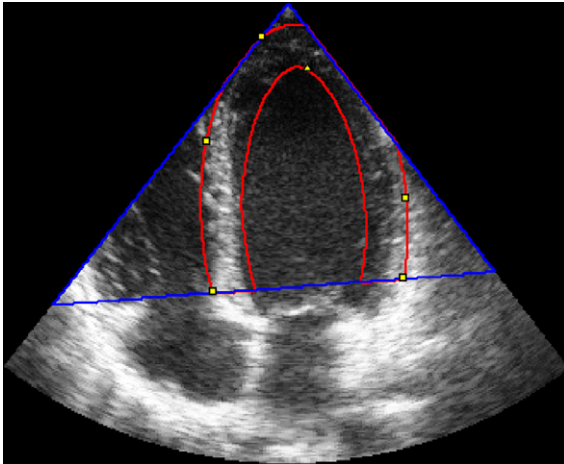


Fig. 7. Definition of the ROI mask. ROI mask for a parasternal short-axis (a), parasternal long-axis (b), apical 4-chamber (c) and apical 2-chamber (d) views and the corresponding image (e), (f), (g) and (h). The evolving curve is shown in red, the ROI in green and the intersection points used for the fit of the two semi-circles are the blue dots. (For interpretation of the references to colour in this figure legend, the reader is referred to the web version of this article.)



**Fig. 8.** Example of initialisation. Yellow dots: Initial points; red: corresponding ellipses; blue: ROI. (For interpretation of the references to colour in this figure legend, the reader is referred to the web version of this article.)

or top side of the image respectively (see Fig. 7f–h). It is thus necessary to define different regions according to the presence or absence of the left ventricle and of image information. The user is thus asked to give two points corresponding to the position of the valves and a mask is then created. This mask defines 3 regions as follows:

- possible presence of the left ventricle and image information is available (for example area 1 in Fig. 7b). In this region both the data attachment term and the shape prior term are used for the evolution of the level-set function.
- possible presence of the left ventricle but outside of the imaged sector (for example area 2 in Fig. 7b). In this region only the shape prior term is used for the evolution of the level-set function.
- left ventricle is absent (for example area 3 in Fig. 7b). Two half circles are fitted on the 4 intersection points between the evolving curve and the ROI (blue points in Fig. 7b), in order to get a closed contour with similar shape as the left ventricle.

Note that in the particular case of parasternal short-axis views, the area 3 is not used (as shown in Fig. 7a and e).

#### 4.4. Initialization procedure

Finally, let us note that the adoption of a localized framework of (Lankton and Tannenbaum, 2008) imposes an initialisation not too far from the desired solution, in order to obtain meaningful results.

**Table 1**  
Results of the fit of the different priors on the mean curve of the epicardial border in term of Dice criteria, Hausdorff distance (HD) and Mean Absolute Distance (MAD). HD and MAD are given in mm.

	Hyperquadrics, $N_h = 4$			Hyperquadrics, $N_h = 6$			Ellipse			3rd order hyperbola		
	Dice	MAD	HD	Dice	MAD	HD	Dice	MAD	HD	Dice	MAD	HD
Parasternal short-axis	0.991 (0.005)	0.244 (0.189)	0.731 (0.409)	0.994 (0.002)	0.168 (0.089)	0.599 (0.224)	0.988 <sup>a</sup> (0.004)	0.321 <sup>a</sup> (0.161)	0.974 <sup>a</sup> (0.379)	0.964 <sup>a</sup> (0.005)	0.963 <sup>a</sup> (0.386)	3.41 <sup>a</sup> (1.12)
Parasternal long-axis	0.995 (0.002)	0.11 (0.058)	1.15 (0.593)	0.992 <sup>a</sup> (0.005)	0.179 <sup>a</sup> (0.12)	1.7 <sup>a</sup> (0.968)	0.989 <sup>a</sup> (0.004)	0.269 <sup>a</sup> (0.104)	2.63 <sup>a</sup> (1.11)	0.986 <sup>a</sup> (0.004)	0.316 <sup>a</sup> (0.111)	2.29 <sup>a</sup> (0.75)
Apical 4-chamber	0.991 (0.005)	0.266 (0.119)	1.73 (0.888)	0.984 (0.024)	0.498 (0.814)	2.67 (2.89)	0.985 <sup>a</sup> (0.005)	0.442 <sup>a</sup> (0.176)	2.3 <sup>a</sup> (1.08)	0.968 <sup>a</sup> (0.005)	0.91 <sup>a</sup> (0.207)	4.6 <sup>a</sup> (0.895)
Apical 2-chamber	0.991 (0.003)	0.258 (0.078)	1.54 (0.6)	0.986 <sup>a</sup> (0.016)	0.442 <sup>a</sup> (0.442)	2.4 <sup>a</sup> (2.16)	0.981 <sup>a</sup> (0.004)	0.573 <sup>a</sup> (0.118)	2.54 <sup>a</sup> (0.617)	0.966 <sup>a</sup> (0.006)	1 <sup>a</sup> (0.223)	5.86 <sup>a</sup> (1.29)

<sup>a</sup> Difference was found significant ( $p < 0.001$ ) when compared to hyperquadrics with  $N_h = 4$ .

The following procedure is thus considered to initialize our algorithm. The user is asked to position only six points. Five points are first positioned near the epicardium. These 5 points are used to fit an initial ellipse (one ellipse is uniquely defined by 5 points). Note that for parasternal long-axis and apical views the two first points are also used to define the ROI as explained in Section 4.3. One last point is then positioned near the endocardium and is used to obtain a second concentric ellipse. The accuracy to which these initial points have to be placed to yield a satisfactory segmentation corresponds to the size of the local data-attachment term of Lankton's energy functional and thus to the radius  $R_N$  of the localizing mask  $N(\mathbf{x})$ . As mentioned in the previous sections,  $R_N$  is set to 15 pixels in our application. These initial points are displayed in yellow in the segmentation examples given in the result section. Fig. 8 shows an apical 4-chamber view with the 6 points given by the user and the corresponding initial ellipses.

Note that providing 6 points is still a reasonable interaction, since the cardiologist usually inputs 30 points (on average) to draw the references. Thus this procedure divides the user interaction by 5. Furthermore cardiologists do not have to be as accurate as they would have to be if they were drawing the final contour. It can also be noted that the proposed algorithm can be used as an initialisation for a tracking algorithm, such as the ones proposed in Comaniciu et al. (2004) and Sühling et al. (2005), reducing thereby the user-interaction (for instance 18 points are required to initialize the tracking of the endocardium in Comaniciu et al., 2004).

## 5. Experiments

### 5.1. Experimental data

In this section, we will evaluate the performance of the proposed algorithm on a dataset of echocardiographic images. The dataset is composed of 80 images acquired from 20 healthy volunteers and taken at End-Diastole (ED) and End-Systole (ES), which are the instants in the cardiac cycle used by cardiologists in routine echocardiography for the diagnosis of pathologies. The data are distributed as follows:

- 7 ED and 8 ES images in parasternal short-axis view,
- 13 ED and 11 ES images in parasternal long-axis view,
- 13 ED and 12 ES in apical 4-chamber view,
- 8 ED and 8 ES images in apical 2-chamber view.

The images in parasternal short-axis views were acquired using a Toshiba Powervision 6000 (Toshiba Medical Systems Europe, Zoetermeer, the Netherlands) equipped with a 3.75 MHz-probe, while the scans from the other views were acquired using a GE

**Table 2**

Results of the fit of the different priors on the mean curve of the endocardial border in term of Dice criteria, Hausdorff distance (HD) and Mean Absolute Distance (MAD). HD and MAD are given in mm.

	Hyperquadrics, $N_h = 4$			Hyperquadrics, $N_h = 6$			Ellipse			3rd order hyperbola		
	Dice	MAD	HD	Dice	MAD	HD	Dice	MAD	HD	Dice	MAD	HD
Parasternal short-axis	0.991 (0.003)	0.142 (0.063)	0.496 (0.168)	0.991 (0.002)	0.149 (0.058)	0.52 <sup>a</sup> (0.128)	0.984 <sup>a</sup> (0.005)	0.281 <sup>a</sup> (0.157)	0.872 <sup>a</sup> (0.434)	0.963 <sup>a</sup> (0.004)	0.604 <sup>a</sup> (0.206)	2.17 <sup>a</sup> (0.84)
Parasternal long-axis	0.99 (0.006)	0.195 (0.115)	1.52 (0.669)	0.984 <sup>a</sup> (0.012)	0.309 <sup>a</sup> (0.212)	2.21 <sup>a</sup> (1.08)	0.984 <sup>a</sup> (0.006)	0.322 <sup>a</sup> (0.137)	2.65 <sup>a</sup> (1.09)	0.963 <sup>a</sup> (0.029)	0.674 <sup>a</sup> (0.473)	3.46 <sup>a</sup> (1.97)
Apical 4-chamber	0.974 (0.018)	0.515 (0.341)	2.14 (1.17)	0.922 <sup>a</sup> (0.055)	1.62 <sup>a</sup> (1.1)	5.84 <sup>a</sup> (3.06)	0.974 (0.009)	0.514 (0.198)	2.18 (0.597)	0.961 <sup>a</sup> (0.011)	0.789 <sup>a</sup> (0.296)	4.23 <sup>a</sup> (1.79)
Apical 2-chamber	0.96 (0.019)	0.809 (0.339)	3.1 (1.21)	0.906 <sup>a</sup> (0.050)	2.03 <sup>a</sup> (0.951)	6.8 <sup>a</sup> (2.87)	0.957 (0.010)	0.901 (0.22)	3.43 <sup>a</sup> (0.866)	0.933 <sup>a</sup> (0.027)	1.49 <sup>a</sup> (0.706)	8.7 <sup>a</sup> (4.93)

<sup>a</sup> Difference was found significant ( $p < 0.001$ ) when compared to hyperquadrics with  $N_h = 4$ .

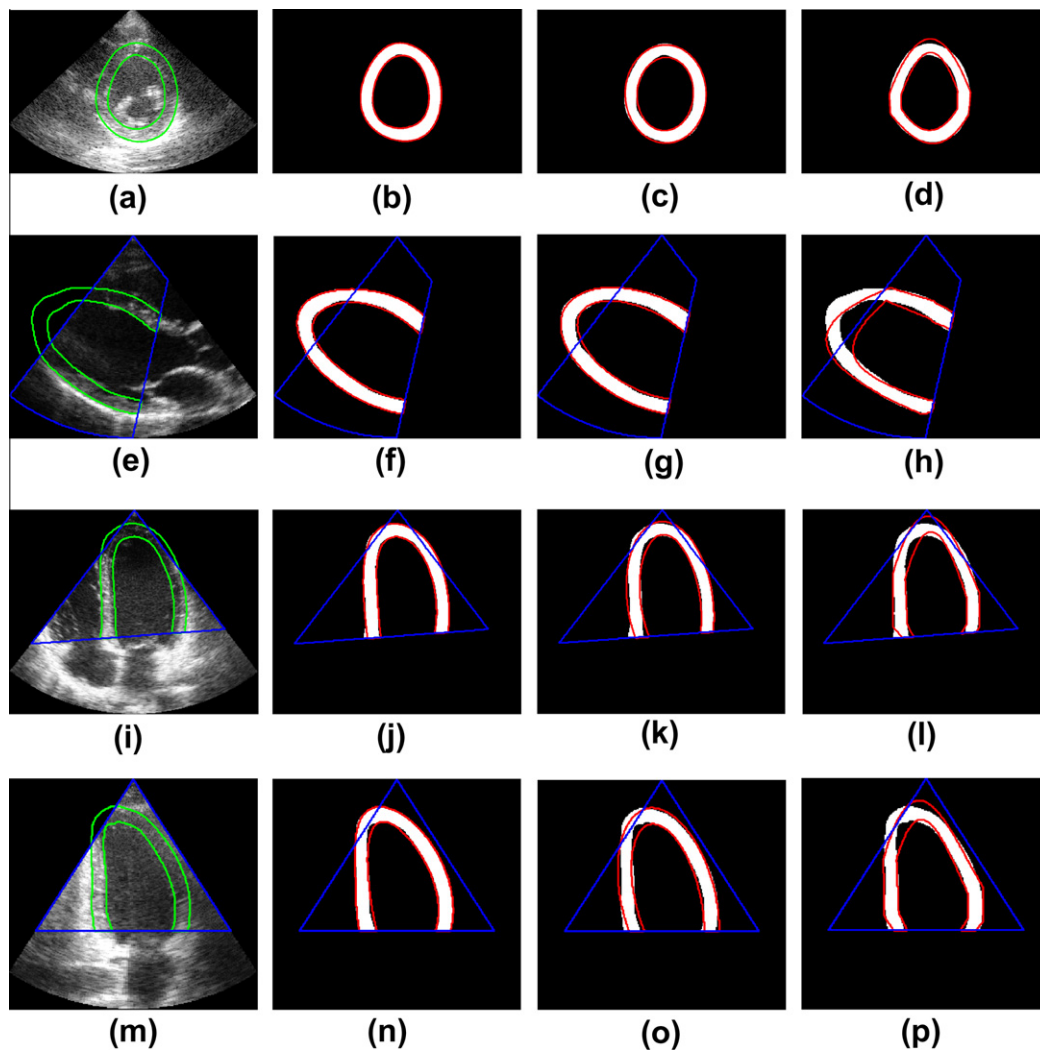


**Fig. 9.** Example of results of fits of the different models with the mean expert curve for the 4 main views (from top to bottom: parasternal short-axis, parasternal long-axis, apical 4-chamber, apical 2-chamber). The fitted model is (from left to right) a hyperquadric with  $N_h = 4$ , an ellipse and a 3rd order hyperbola. The blue contour corresponds to the ROI, the green to the reference and the red to the fit result. (For interpretation of the references to colour in this figure legend, the reader is referred to the web version of this article.)

Vivid E9 system equipped with a 2.5 MHz M5S probe (GE Vingmed Ultrasound, Horten, Norway).

### 5.2. Error measures

Manual segmentation drawn by three expert cardiologists was used as reference. To evaluate segmentation results we measured

the correspondence between the detected contours and the manual references given by the expert cardiologists. In particular we adopt three different metrics, *i.e.* the Dice coefficient  $D$  (Dice, 1945), the Mean Absolute Distance MAD (expressed in mm) (Comaniciu et al., 2004) and the Hausdorff distance  $HD$  (expressed in mm) (Huttenlocher et al., 1993). If we call with  $R$  and  $S$  the reference contour and the detected one, and introduce the generic

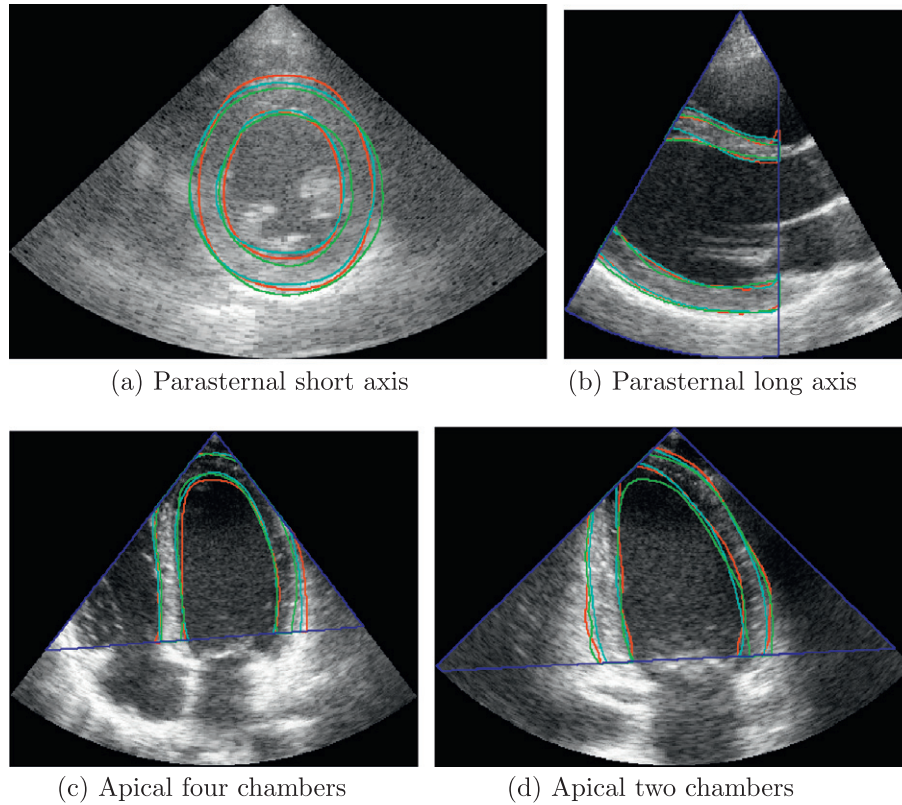


**Fig. 10.** References from the two expert cardiologists in the different views. In red: expert 1, in green: expert 2, in cyan: expert 3 and in blue the region of interest. (For interpretation of the references to colour in this figure legend, the reader is referred to the web version of this article.)

points  $r$  and  $s$  belonging to  $R$  and  $S$  respectively, then the Mean Absolute Distance and the Hausdorff distance are defined as:

$$MAD(R, S) = \frac{1}{N} \sum_s |d(s, R)|, \quad (19)$$

and

$$HD(R, S) = \max(\sup_{r \in R} d(r, S); \sup_{s \in S} d(s, R)) \quad (20)$$

where  $d(a, A)$  represents the shortest distance from the point  $a$  to the curve  $A$  and  $N$  is the number of points in the contour. While the MAD measures a global correspondence between the two contours, the Hausdorff distance is well suited for evaluating the local behavior of the algorithm. Moreover, by defining  $\Omega_S$  and  $\Omega_R$  the sets of pixels within the segmented and the reference region, the Dice coefficient writes as:

$$Dice(\Omega_R, \Omega_S) = \frac{2Area(\Omega_S \cap \Omega_R)}{Area(\Omega_R) + Area(\Omega_S)}. \quad (21)$$

This coefficient measures the correspondence between the two regions, and varies from 0 to 1: it is 1 when the two regions are coincident and 0 when they have null intersection. Note that all these measures are only computed inside the ROI.

The method is also compared with a recent algorithm proposed by (Hamou and El-Sakka, 2010), who uses optical flow and a shape prior as external energies within a GVF snake framework. The prior is obtained by fitting two 3rd order hyperbola, one on the 2/3 upper part of the contour and the other one on the 1/3 lower part. This method was chosen for comparison purposes because it also uses a geometrical shape prior that can thus be applied to any view.

### 5.3. Shape prior validation

To validate the choice of our shape prior, we fitted four different models (hyperquadrics with  $N_h = 4$  and 6 terms, ellipses and the 3rd order hyperbola model of Hamou and El-Sakka (2010)) on the mean curve of the manual references drawn by three expert cardiologists on the dataset. The mean curve is obtained following the method described in (Chalana and Kim, 1997). The results are given in Tables 1 and 2 and some examples of fits are displayed in Fig. 9.

From these two tables, we can see that the proposed hyperquadric with  $N_h = 4$  is able to model the heart boundaries with a good accuracy. Indeed the MAD values are always below 0.9 mm for the endocardial fit and below 0.3 mm for the epicardial fit, which shows that the prior is on average really close to the cardiologist's references. If we consider the Hausdorff distance, which is more sensitive to local errors, it can be observed that the maximal fitting error is never larger than 3.1 mm for the endocardial border and 1.8 mm for the epicardial border. This indicates that even locally, our model is close to the experts' boundaries.

Tables 1 and 2 also indicate that the hyperquadrics with  $N_h = 4$  always performs better than the one proposed by Hamou and El-Sakka (2010). The Hausdorff distance and MAD values associated to the proposed prior are on average 30% lower, which shows that our prior is better suited for the modelling of heart boundaries. This can be explained by the fact that hyperquadrics can model asymmetries which is not the case for the 3rd order hyperbola as it can be observed in Fig. 9. Note that the above mentioned differences were found to be statistically significant for any view with a level  $p = 0.001$  using the Friedman rank test.

If we now compare hyperquadrics with  $N_h = 4$  to ellipses, we can draw almost the same conclusion except for the endocardial border

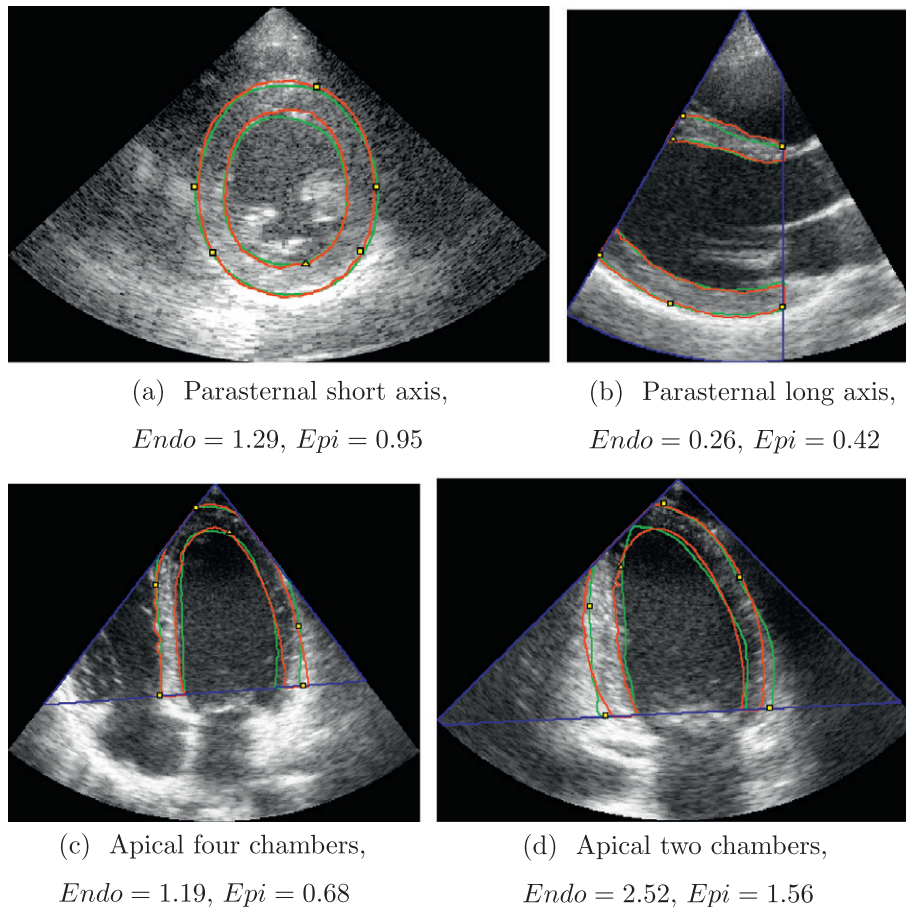


**Fig. 11.** Results of segmentation of our method on end-diastolic images. In blue the region of interest, in green the mean reference of the cardiologist, in red our contour. The yellow dots are the 6 points given by a third expert. For each view, the MAD (in mm) computed between the segmentation result and the mean contour is given. (For interpretation of the references to colour in this figure legend, the reader is referred to the web version of this article.)

in apical 2 and 4-chamber views, where hyperquadrics and ellipse yield almost the same results. In particular, it may be noted that even in parasternal short-axis views, where the heart boundaries are usually approximated by ellipses, our model provides better results than ellipses. Since even in this view the expert contours are not exactly ellipses, an elliptical prior will not be able to exactly fit the small deviation from this model while hyperquadrics will.

Finally we can see that using hyperquadrics with  $N_h = 4$  allows to better model the heart shape than when using  $N_h = 6$ : the results are indeed either very close (i.e. no significant statistical difference at a level  $p = 0.001$ ) or hyperquadrics with  $N_h = 4$  performs better when the difference is significant. Note also that  $N_h = 6$  has the drawback to yield a higher computational load since more parameters have to be estimated.

As a conclusion, we will set  $N_h = 4$  for the segmentation experiments to be described in the next sections, which is a good compromise between approximation accuracy and the computational load of the algorithm.

#### 5.4. Myocardial segmentation

We evaluate in this section the performance of our segmentation algorithm. The segmentation was performed using the parameters given in Section 4 and the 6 points required for the initialisation were provided by a fourth cardiologist.

In Fig. 10, we show an example of the references from the three experts in order to illustrate the inter-observer variability. We show in Figs. 11 and 12 the corresponding segmentation results,

the reference contour and the error measures on end-diastolic (ED) and end-systolic (ES) images respectively.

Tables 3 and 4 provide the mean and standard deviation of the error measures obtained for the complete data set on epicardial and endocardial borders, respectively. In each table, we give the error measures associated to the Inter-observer Distance (IOD, three first columns), the proposed method (three middle columns) and the error measures obtained by using Hamou's method (three last columns).

Concerning the proposed approach, the segmentation of the epicardial border in the parasternal short-axis view (first line in Table 3) yields a large value for the Dice (0.961) and accordingly a small value for the MAD (1.07 mm). While the Dice and MAD allow evaluating the global quality of the segmentation, the HD provides an upper bound on the error and is 2.96 mm for this orientation. The comparison of these values with the corresponding IOD (three first columns in Table 3) allows interpreting them in a relative perspective. For the parasternal short-axis view, it may be observed that the Dice obtained using the proposed method is slightly larger than the inter-observer Dice (0.952) and that the MAD and HD are slightly lower than the corresponding inter-observer values (1.41 mm and 3.62 mm, respectively). This thus indicates that the segmentation provides consistent results in the sense that the difference with the experts' reference is comparable to or even smaller than the distance between experts.

The results associated with the endocardial borders in the same parasternal short-axis view (first line in Table 4), show that the errors are in the same order and slightly larger: 0.926 for the Dice,

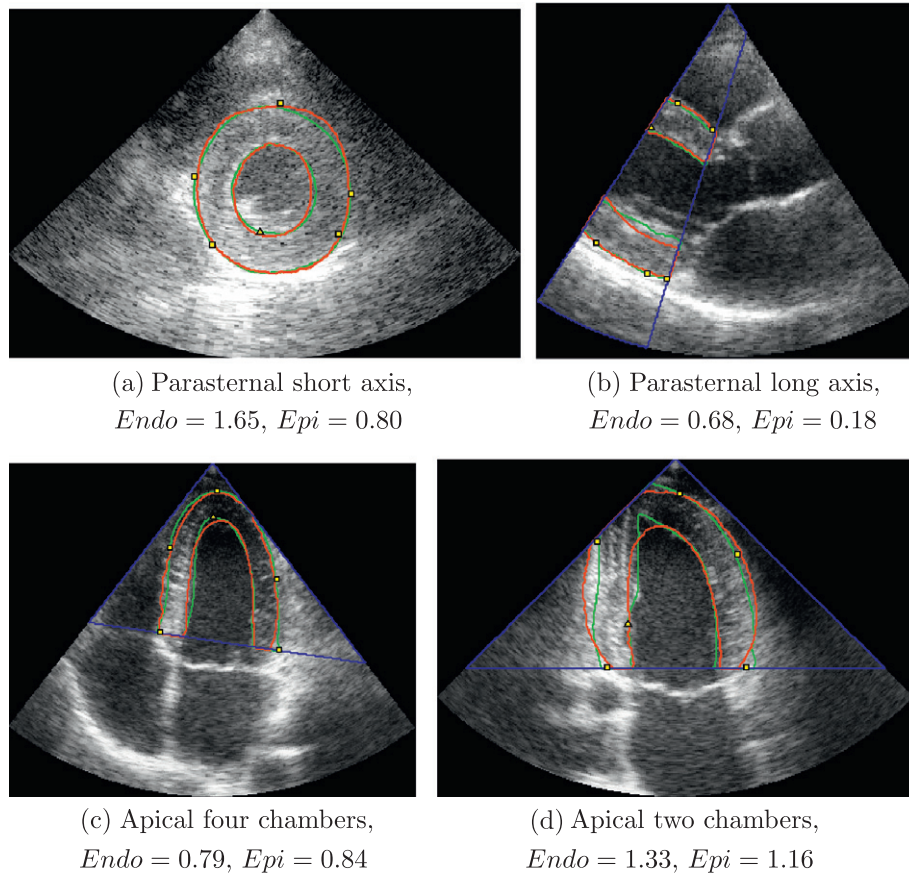


**Fig. 12.** Results of segmentation of our method on end-systolic images. In blue the region of interest, in green the mean reference of the cardiologist, in red our contour. The yellow dots are the 6 points given by a third expert. For each view, the MAD (in mm) computed between the segmentation result and the mean contour is given. (For interpretation of the references to colour in this figure legend, the reader is referred to the web version of this article.)

**Table 3**  
Results of the segmentation of the epicardial border. The results of our method and the one described in Hamou and El-Sakka (2010) as well as the Inter-Observers Distance (IOD) are shown in term of Dice criteria, Mean Absolute Distance (MAD) and Hausdorff distance (HD). The given values correspond to the mean (Standard deviation). HD and MAD are given in mm.

	IOD			Our method			Hamou		
	Dice	MAD	HD	Dice	MAD	HD	Dice	MAD	HD
Parasternal short-axis	0.952 (0.017)	1.41 (0.754)	3.62 (1.86)	0.961 (0.011)	1.07 (0.518)	2.96 (1.23)	0.936 <sup>a</sup> (0.028)	1.51 <sup>a</sup> (0.387)	4.35 <sup>a</sup> (1.23)
Parasternal long-axis	0.98 (0.008)	0.484 (0.197)	3.77 (1.96)	0.982 (0.006)	0.418 (0.13)	2.75 (0.686)	0.958 <sup>a</sup> (0.032)	0.991 <sup>a</sup> (0.651)	4.98 <sup>a</sup> (2.43)
Apical 4-chamber	0.952 (0.023)	1.41 (0.679)	4.64 (2.06)	0.959 (0.011)	1.18 (0.287)	4.41 (1.15)	0.948 <sup>a</sup> (0.015)	1.54 <sup>a</sup> (0.435)	6.23 <sup>a</sup> (1.59)
Apical 2-chamber	0.949 (0.024)	1.59 (0.691)	5.78 (1.83)	0.941 (0.022)	1.85 (0.694)	6.06 (1.38)	0.935 <sup>a</sup> (0.019)	2.06 <sup>a</sup> (0.543)	7.74 (2.02)

<sup>a</sup> Difference was found significant ( $p < 0.05$ ) when compared to our method.

1.25 mm for the MAD and 2.87 mm for the HD. These values are also in the same order and slightly better than the corresponding IOD (0.917 for the Dice, 1.46 mm for the MAD and 3.28 mm for the HD). This is linked to the fact that the segmentation of the endocardial border is generally less smooth than the epicardial one and moreover implies exclusion of the papillary muscles present in the image.

Considering now the 3 other orientations (lines 2–4 in Tables 3 and 4), a variation in the performances may be observed. The results obtained for the parasternal views are better than the results corresponding to the apical view: considering the MAD and

the epicardial border (Table 3, fifth column), the observed values are 1.07 mm and 0.418 mm for the parasternal short-axis and long-axis views, whereas they are 1.18 mm and 1.85 mm for the apical 4-chambers and 2-chambers views. The same trend holds for the endocardial border (Table 4, fifth column) and the other error measures (Dice and HD, fourth and sixth columns). This situation is linked to the variations in image quality and content, as illustrated in Figs. 11 and 12: while the regions corresponding to the myocardium are well-defined in parasternal views (Fig. 11a and b, Fig. 12a and b), in the apical views the region of the apex is commonly located in the near field of the probe (Fig. 11c and

**Table 4**

Results of the segmentation of the endocardial border. The results of our method and the one described in Hamou and El-Sakka (2010) as well as the Inter-Observers Distance (IOD) are shown in term of Dice criteria, Mean Absolute Distance (MAD) and Hausdorff distance (HD). The given values correspond to the mean (standard deviation). HD and MAD are given in mm.

	IOD			Our method			Hamou		
	Dice	MAD	HD	Dice	MAD	HD	Dice	MAD	HD
Parasternal short-axis	0.917 (0.032)	1.46 (0.658)	3.28 (1.35)	0.926 (0.040)	1.25 (0.693)	2.87 (1.4)	0.869 <sup>a</sup> (0.090)	2.01 <sup>a</sup> (1.24)	4.33 <sup>a</sup> (1.71)
Parasternal long-axis	0.959 (0.023)	0.792 (0.41)	3.85 (1.62)	0.955 (0.035)	0.818 (0.559)	3.32 (1.49)	0.918 <sup>a</sup> (0.050)	1.6 <sup>a</sup> (0.778)	6.13 <sup>a</sup> (2.08)
Apical 4-chamber	0.938 (0.031)	1.27 (0.535)	4.66 (2)	0.929 (0.026)	1.48 (0.554)	4.88 (1.47)	0.9 <sup>a</sup> (0.045)	2.2 <sup>a</sup> (1)	7.82 <sup>a</sup> (3.46)
Apical 2-chamber	0.907 (0.051)	1.9 (0.871)	5.91 (2.16)	0.887 (0.046)	2.44 (0.946)	6.77 (1.71)	0.836 <sup>a</sup> (0.065)	3.83 <sup>a</sup> (1.53)	10.6 <sup>a</sup> (4.31)

<sup>a</sup> Difference was found significant ( $p < 0.05$ ) when compared to our method.

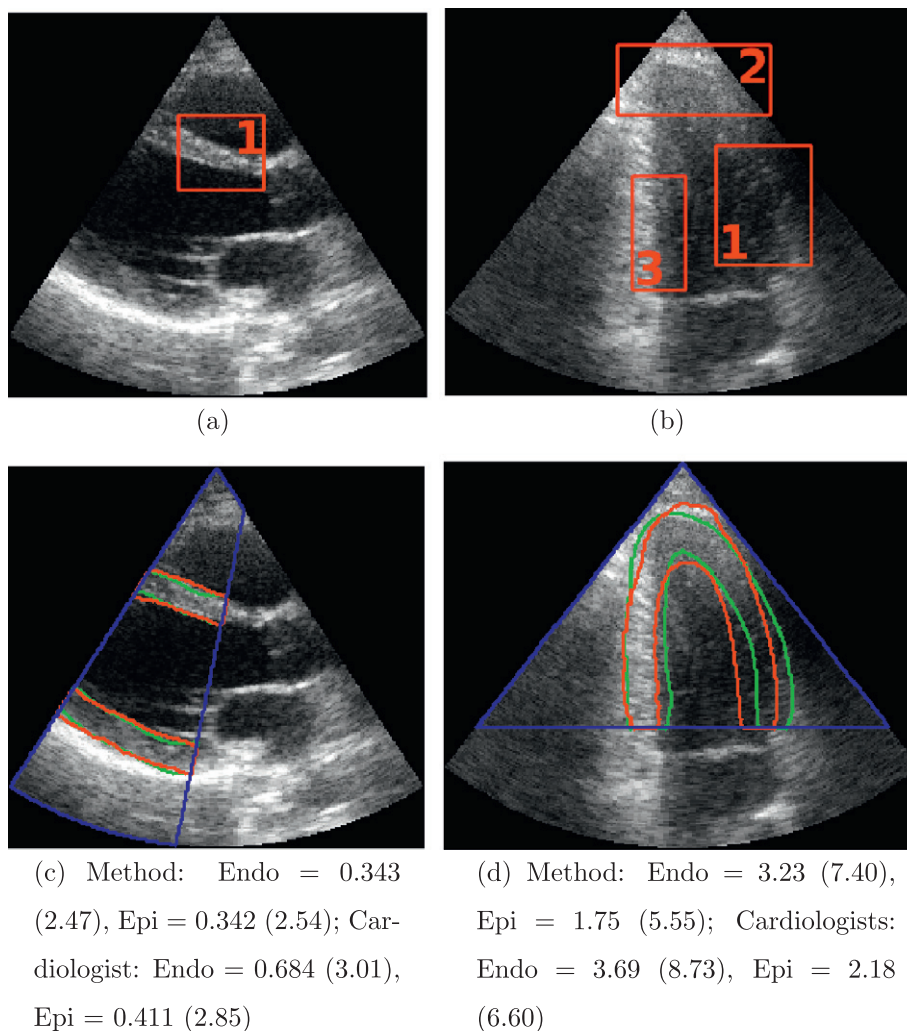


**Fig. 13.** Top row: long-axis and apical 2-chamber view images; bottom row: segmentation result on the same image as (a) and (b). Red: segmentation result; green: mean reference contour; blue ROI. For each segmentation result, we give the MAD (HD) value in mm for the proposed method and the cardiologists. (For interpretation of the references to colour in this figure legend, the reader is referred to the web version of this article.)

d, Fig. 12c and d) and is thus usually blurred, yielding missing boundaries of significant size. In these cases, the shape prior is able to cope with this missing information and to provide meaningful results, but induces a lower accuracy.

The standard deviation for the epicardial border varies between  $6 \times 10^{-3}$  and 0.022 for the Dice criterion, 0.13 and 0.694 for the

MAD and 0.686 and 1.38 for the HD. These values are in the same order than the standard deviation obtained for the experts' outline boundaries, showing that the segmentation results do not deviate from the mean value more than the experts' outlined boundaries do. The same conclusion can be drawn for the endocardial detection where the standard deviation varies between 0.026 and 0.046 for

the Dice criterion, 0.554 and 0.946 for the MAD and 1.4 and 1.71 for the HD.

To illustrate the quality of the results, we show in Fig. 13 one of the best and one of the worst results of the algorithm, along with the corresponding error measures (MAD and Hausdorff) and the inter-observer variability. The good result was obtained from a parasternal long-axis image with a good image quality and where both borders can clearly be seen. Indeed the contrast between the myocardium muscle and the blood pool or the surrounding tissue is very high (area 1 of Fig. 13a), there is no shadowing artifact, yielding a proper segmentation.

On the other hand, when dealing with an image of bad quality, where part of the myocardium is occluded (area 1 of Fig. 13b) or in the near field area of the probe (area 2 of Fig. 13b), the segmentation is worsened as can be seen in the apical 2-chamber view (Fig. 13d). Indeed in those area, the statistics of the inside and outside are identical and thus the level set does not evolve. Moreover, the contour has been attracted to an intensity variation inside the septum wall (area 3 of Fig. 13b), that is greater than the intensity difference between the septum wall and the blood pool.

Consistently, it may be observed that the errors measures are higher for the bad quality image. It is also to be noted that these errors are on the same order than the inter-observer variability, confirming the difficulty of such image and showing that the algorithm provides results with an accuracy comparable to the one associated to the cardiologists.

The results provided in the last three columns in Tables 3 and 4 allow comparing the performance of the proposed method and Hamou's method. These results show that our method always yields better performance. Considering the mean differences between the error measures associated with the two approaches, the HD of our method is 1.5 mm lower and the MAD is 0.5 mm lower which corresponds to at least a 25% improvement of the result. This can be explained by the fact that our shape prior is better suited for the modelling of the heart boundaries as was shown in Section 5.3. This allows our segmentation algorithm to better handle missing boundaries or intensity inhomogeneities inside the myocardium. Note that all these differences has been found to be statistically significant at a level  $p = 0.05$  using the Friedman rank test, except for the Hausdorff distance evaluated on the epicardial contour in the apical 2-chamber view, where the two methods performs similarly.

It has to be noted that the six points used for the initialisation of the algorithm often belong to the segmentation results (as shown in Figs. 11 and 12). This can be simply explained by the fact that the initial points are generally put by experts in regions where it is easy to delineate the myocardial border, which corresponds to regions with high contrast. Thus the evolving contour does not move far away from those points.

As a final remark, let us note that the computational time required for one segmentation varies between 30 s and 1 min, with a non-optimized Matlab implementation ran on a 3.06 GHz Core Duo laptop, with 3.9 GB RAM running Fedora 14.

## 6. Conclusion

In this work, we presented a new algorithm that allows segmenting the whole myocardium for the four main views used in clinical routine. We approximated the heart boundaries by two hyperquadrics that are then used as a shape prior for the evolving contour. Our method showed good results when compared with expert segmentation on a database composed of 80 images with clinical interest. Further work will focus on the use of this algorithm to segment whole sequences.

## Acknowledgments

This work was partially supported by Agence Nationale de la Recherche US-Tagging grant), the region Rhône-Alpes (ExploraDoc and AccueilDoc grants) and Egide (PHC Tournesol grant). We thank Dr. Oana Savu, Dr. Ruta Jasaityte and Dr. Anca Florian from Cardiovascular Imaging and Dynamics lab (Leuven) for providing the expert's contours.

## Appendix A. Derivation of the Thickness term

Let us first recall our thickness energy:

$$\begin{aligned} E(\phi) &= \int_{\Omega} \phi(\mathbf{x} + R_T \mathbf{N}) \cdot H(\phi(\mathbf{x} + R_T \mathbf{N})) \cdot \delta(\phi(\mathbf{x})) \, d\mathbf{x} \\ &= \int_{\Omega} L(\mathbf{x}, \phi(\mathbf{x})) \, d\mathbf{x}. \end{aligned} \quad (\text{A.1})$$

To minimize this energy and obtain the evolution term, we derive  $L$  with respect to  $\phi$ , using variational calculus and the Euler–Lagrange theorem:

$$\begin{aligned} \frac{\partial L(\phi)}{\partial \phi} &= \frac{\partial}{\partial \phi} \phi(\mathbf{x}^*) \cdot H(\phi(\mathbf{x}^*)) \cdot \delta(\phi(\mathbf{x})) + \phi(\mathbf{x}^*) \cdot \frac{\partial}{\partial \phi} H(\phi(\mathbf{x}^*)) \\ &\quad \cdot \delta(\phi(\mathbf{x})) + \phi(\mathbf{x}^*) \cdot H(\phi(\mathbf{x}^*)) \cdot \frac{\partial}{\partial \phi} \delta(\phi(\mathbf{x})), \end{aligned} \quad (\text{A.2})$$

where  $\mathbf{x}^* = \mathbf{x} + R_T \mathbf{N}$ .

As in Lankton and Tannenbaum (2008), we made the assumption that  $\frac{\partial}{\partial \phi} \delta(\phi(\mathbf{x})) \simeq 0$  near the zero-level and thus should not affect the evolution process. Thus Eq. (A.2) rewrites as:

$$\frac{\partial L(\phi)}{\partial \phi} = \frac{\partial}{\partial \phi} \phi(\mathbf{x}^*) \cdot \delta(\phi(\mathbf{x})) \cdot [H(\phi(\mathbf{x}^*)) + \phi(\mathbf{x}^*) \cdot \delta(\phi(\mathbf{x}^*))]. \quad (\text{A.3})$$

Since  $\frac{\partial}{\partial \phi} \phi(\mathbf{x}^*) = 1$  and

$$\begin{cases} \delta(\phi(\mathbf{x}^*)) = 1, & \text{if } \phi(\mathbf{x}^*) = 0 \\ \delta(\phi(\mathbf{x}^*)) = 0, & \text{otherwise} \end{cases} \iff \phi(\mathbf{x}^*) \cdot \delta(\phi(\mathbf{x}^*)) = 0, \forall \mathbf{x}^* \quad (\text{A.4})$$

we obtain

$$\frac{\partial L(\phi)}{\partial \phi} = H(\phi(\mathbf{x} + R_T \mathbf{N})) \cdot \delta(\phi(\mathbf{x})). \quad (\text{A.5})$$

Thus we get

$$\frac{\partial L(\phi)}{\partial \phi} = 0 \iff H(\phi(\mathbf{x} + R_T \mathbf{N})) \cdot \delta(\phi(\mathbf{x})) = 0, \quad (\text{A.6})$$

and the related evolution equation is thus given by

$$\frac{\partial \phi}{\partial \tau} = -H(\phi(\mathbf{x} + R_T \mathbf{N})) \cdot \delta(\phi(\mathbf{x})). \quad (\text{A.7})$$

## References

- Abdallah, A., Ghorbel, F., Chatti, K., Essabbah, H., Bedoui, M., 2010. A new uniform parameterization and invariant 3D spherical harmonic shape descriptors for shape analysis of the heart's left ventricle – a pilot study. *Pattern Recogn. Lett.* 31 (13), 1981–1990.
- Alessandrini, M., Dietenbeck, T., Barbosa, D., D'hooge, J., Basset, O., Speciale, N., Friboulet, D., Bernard, O., 2010. Segmentation of the full myocardium in echocardiography using constrained level-sets. In: *Computing in Cardiology*, Belfast, Northern Ireland, UK.
- Alessandrini, M., Friboulet, D., Basset, O., D'hooge, J., Bernard, O., 2009. Level-set segmentation of myocardium and epicardium in ultrasound images using localized bhattacharyya distance. In: *IEEE International Ultrasonics Symposium*, Roma, Italy, pp. 2468–2471.
- Berg, J.M., 1998. On parameter estimation using level sets. *SIAM J. Control Optim.* 37, 1372–1393.

- Bosch, J., Mitchell, S., Lelieveldt, B., Nijland, F., Kamp, O., Sonka, M., Reiber, J., 2002. Automatic segmentation of echocardiographic sequences by active appearance motion models. *IEEE Trans. Med. Imag.* 21, 1374–1383.
- Carneiro, G., Nascimento, J.C., Freitas, A., 2010. Robust left ventricle segmentation from ultrasound data using deep neural networks and efficient search methods. In: *IEEE International Symposium on Biomedical Imaging (ISBI)*, Rotterdam, The Netherlands.
- Caselles, V., Kimmel, R., Sapiro, G., 1997. Geodesic active contours. *Int. J. Comput. Vis.* 22, 61–79.
- Chalana, V., Kim, Y., 1997. A methodology for evaluation of boundary detection algorithms on medical images. *IEEE Trans. Med. Imag.* 16 (5), 642–652.
- Chalana, V., Linker, D., Haynor, D., Kim, Y., 1996. A multiple active contour model for cardiac boundary detection on echocardiographic sequences. *IEEE Trans. Med. Imag.* 15 (3), 290–298.
- Chan, T., Vese, L., 2001. Active contours without edges. *IEEE Trans. Image Process.* 10, 266–277.
- Chen, T., Babb, J., Kellman, P., Axel, L., Kim, D., 2008. Semiautomated segmentation of myocardial contours for fast strain analysis in cine displacement-encoded mri. *IEEE Trans. Med. Imag.* 27 (8), 1084–1094.
- Chen, Y., Huang, F., Tagare, H.D., Rao, M., 2007. A coupled minimization problem for medical image segmentation with priors. *Int. J. Comput. Vis.* 71 (3), 259–272.
- Chen, Y., Tagare, H.D., Thiruvankadam, S., Hunag, F., Wilson, D., Gopinath, K.S., Briggs, R.W., Geiser, E.A., 2002. Using prior shapes in geometric active contours in a variational framework. *Int. J. Comput. Vis.* 50, 315–328.
- Cohen, I., Cohen, L., 1996. A hybrid hyperquadric model for 2-D and 3-D data fitting. *Comput. Vis. Image Understand.* 63 (3), 527–541.
- Comanicu, D., Zhou, X.S., Krishnan, S., 2004. Robust real-time myocardial border tracking for echocardiography: an information fusion approach. *IEEE Trans. Med. Imag.* 23, 849–860.
- Cong, G., Parvin, B., 2000. Model-based segmentation of nuclei. *Pattern Recogn.* 33 (8), 1383–1393.
- Dias, J.M.B., Leitao, J.M.N., 1996. Wall position and thickness estimation from sequences of echocardiographic images. *IEEE Trans. Med. Imag.* 15, 25–38.
- Dice, L., 1945. Measures of the amount of ecologic association between species. *Ecology* 26, 297–302.
- Dietenbeck, T., Alessandrini, M., Barbosa, D., D'hooge, J., Friboulet, D., Bernard, O., 2011. Multiview myocardial segmentation in echocardiographic images using a piecewise parametric shape prior. In: *IEEE International Symposium on Biomedical Imaging (ISBI)*, Chicago, USA, 645–648.
- Duan, Q., Angelini, E.D., Laine, A.F., 2009. Surface function actives. *J. Vis. Commun. Image R.* 20 (7), 478–490.
- Hamou, A., El-Sakka, M., 2010. Optical flow active contours with primitive shape priors for echocardiography. *EURASIP J. Adv. Signal Process.*, 2010.
- Hanson, A., 1988. Hyperquadrics: smoothly deformable shapes with convex polyhedral bounds. *CVGIP* 44, 191–210.
- Huttenlocher, D., Klanderma, G., Rucklidge, W., 1993. Comparing images using the Hausdorff distance. *IEEE Trans. Pattern Anal. Machine Intell.* 15 (9), 850–863.
- Kumar, S., Han, S., Goldgof, D., Bowyer, K., 1995. On recovering hyperquadrics from range data. *IEEE Trans. Pattern Anal. Machine Intell.* 17, 1079–1083.
- Lankton, S., Tannenbaum, A., 2008. Localizing region-based active contours. *IEEE Trans. Image Process.* 17, 2029–2039.
- Lelieveldt, B., van der Geest, R., Rezaee, M.R., Bosch, J., Reiber, J., 1999. Anatomical model matching with fuzzy implicit surfaces for segmentation of thoracic volume scans. *IEEE Trans. Med. Imag.* 18 (3), 218–230.
- Leventon, M., Grimson, W., Faugeras, O., 2000. Statistical shape influence in geodesic active contours. In: *Proc. IEEE Conf. Comp. Vision and Patt. Recog.*, pp. 316–323.
- Lin, N., Yu, W., Duncan, J.S., 2003. Combinative multi-scale level set framework for echocardiographic image segmentation. *Med. Image Anal.* 7, 529–537.
- Lynch, M., Ghita, O., Whelan, P., 2006. Left-ventricle myocardium segmentation using a coupled level-set with a priori knowledge. *Comput. Med. Imag. Graph.* 30 (4), 255–262.
- Mignotte, M., Meunier, J., Tardiff, J., 2001. Endocardial boundary estimation and tracking in echocardiographic images using deformable templates and Markov random fields. *Pattern Anal. Appl.* 4, 256–271.
- Noble, J.A., Boukerroui, D., 2006. Ultrasound image segmentation: a survey. *IEEE Trans. Med. Imag.* 25 (11), 987–1010.
- Orderud, F., Kiss, G., Torp, H.G., 2008. Automated coupled segmentation of endo- and epicardial borders in 3D echocardiography. In: *IEEE Ultrasonics Symposium*.
- Osher, S., Fedkiw, R., 2002. *Level Set Methods and Dynamic Implicit Surfaces*. Springer Verlag.
- Osher, S., Sethian, J., 1988. Fronts propagating with curvature-dependent speed: algorithms based on Hamilton–Jacobi formulation. *J. Comput. Phys.* 79, 12–49.
- Paragios, N., 2002. A variational approach for the segmentation of the left ventricle in cardiac image analysis. *Int. J. Comput. Vis.* 50 (3), 345–362.
- Paragios, N., Jolly, M., Taron, M., Ramaraj, R., 2005. Active shape models and segmentation of the left ventricle in echocardiography. In: *Scale-Space 2005*, LNCS 3459, pp. 131–142.
- Press, W., Teukolsky, S., Vetterling, W., Flannery, B., 1992. *Numerical Recipes in C*. Cambridge. Cambridge Univ. Press, England.
- Robert, A., 1995. Modelization of the left ventricle and its deformations using superquadrics and hyperquadrics. In: *Computer Assisted Radiology (CAR'95)*, Berlin, pp. 189–194.
- Sühling, M., Arigovindan, M., Jansen, C., Hunziker, P., Unser, M., 2005. Myocardial motion analysis from b-mode echocardiograms. *IEEE Trans. Image Process.* 14 (4), 525–536.
- Sussman, M., Fatemi, E., Smereka, P., Osher, S., 1998. An improved level set method for incompressible two-phase flows. *J. Comput. Fluids* 27, 663–680.
- Tao, Z., Tagare, H.D., 2007. Tunneling descent for M.A.P. active contours in ultrasound segmentation. *Med. Image Anal.* 11, 266–281.
- Taron, M., Paragios, N., Jolly, M., 2004. Border detection on short axis echocardiographic views using a region based ellipse-driven framework. In: *MICCAI*, pp. 443–450.
- Zeng, X., Staib, L., Schultz, R., Duncan, J., 1998. Segmentation and measurement of the cortex from 3D MR images. In: *Medical Image Computing and Computer-Assisted Intervention – MICCAI'98*, pp. 519–530.
- Zhu, Y., Papademetris, X., Sinusas, A., Duncan, J., 2009. A dynamical shape prior for LV segmentation from RT3D echocardiography. In: *MICCAI*, pp. 206–213.
- Zhu, Y., Papademetris, X., Sinusas, A.J., Duncan, J.S., 2010. A coupled deformable model for tracking myocardial borders from real-time echocardiography using an incompressibility constraint. *Med. Image Anal.* 14, 429–448.